JOURNAL OF AIRCRAFT
Vol. 29, No. 6, Nov.–Dec. 1992

Propeller Slip-Stream Model in Subsonic Linearized Potential Flow

Per Lötstedt*
SAAB Aircraft Division, SAAB-SCANIA, S-581 88 Linköping, Sweden

A model has been developed for computation of the time-averaged subsonic flowfield over a nacelle and a wing induced by a propeller. The slip-stream model is based on a classical propeller theory and is included in an existing panel program. The geometry of the slip stream is determined by the nacelle. The influence of the propeller is given by a combined momentum-blade element theory. No experimental data is necessary. The computed pressures and velocities are compared to wind-tunnel data for two angles of attack and two geometries: 1) an axisymmetric nacelle and wing, and 2) a nonaxisymmetric nacelle and wing.

I. Introduction

THE prediction of the influence of propeller slip stream on the flow is important in the design phase of a new propeller-driven aircraft. The flow pattern over the nacelle and wing is affected considerably by a tractor propeller mounted on the wing, particularly at take-off conditions. Panel methods are a standard tool for aerodynamical computations around three-dimensional configurations at subsonic speeds, see Ref. 1. Usually panel programs are written to solve potential flow problems but they can be amended to also handle the vortical flow behind a rotating propeller. The advantage of panel methods is that they are easy to use and inexpensive in terms of CPU time. When a propeller slip-stream capability is added to a panel program the extension should also have these two properties. The flow in the slip stream is much more complicated than ordinary freestream flow and simplifications in the computational model are necessary. Therefore, we cannot expect to obtain the same accuracy in the predictions with the slip stream as we are used to without the slip stream. This is also true for wind-tunnel experiments.

In this article we describe a propeller slip-stream model which has been incorporated in an existing panel program.[2] The time-averaged flow behind the propeller is generated by a system of vortices following a classical propeller theory.[3] The strength of the vortices is determined by a combined momentum-blade element theory. The propeller data needed in the simulation are the number of blades, the geometry of the blades, the speed of revolution, etc. No supporting wind-tunnel experiment is necessary. The geometry of the slip stream is approximated taking the surface of the nacelle into account. This is important in order to obtain realistic pressures on the nacelle. The velocities in the slip stream determined by the model are introduced together with the freestream as onset flow in the panel method.

The computed pressures and velocities are compared to wind-tunnel measurements from the FFA.[4,5] The configuration geometries are an axisymmetric nacelle with a wing[5] and a nonaxisymmetric nacelle with a wing.[4] The nonaxisymmetric nacelle is such that the shape of the innermost sections of the slip stream is changed by the presence of the nacelle. The Mach number is 0.15 and the angle-of-attack α is 0 or 5 deg. The chosen propeller data correspond to a takeoff case with a contribution from the slip stream in the freestream direction of more than 60% of the freestream speed. The c_p values on the wing and nacelle and the velocities in the slip stream outside the nacelle are compared. The agreement in the simplest case, the axisymmetric nacelle at $\alpha = 0$ deg, is quite good. In the more complex flows around the nonaxisymmetric nacelle the influence of the slip stream on the wing pressures is overestimated in comparison with the experiments.

The time-averaged flow over a nacelle and wing behind a propeller has been computed previously using panel methods, nonlinear potential equations, and the Euler equations. In Refs. 6–9 a panel method is the basis for the development of the slip-stream model. The slip stream is modeled analytically in Ref. 6. The configuration is a nacelle with a wing. The computed pressures in Ref. 6 are compared to experimental data at the wing. A propeller panel model is presented in Ref. 8. The model is applied in Ref. 9 to a complete aircraft configuration with aft-mounted pusher propellers and the computations are compared to wind-tunnel results. In Ref. 7 the same model is developed to predict the flow over a nacelle and wing behind a tractor propeller. Propeller simulation codes for higher Mach numbers must be based on solvers of nonlinear equations. In Ref. 10 a program for solution of the transonic small perturbation equation is extended to include slip-stream effects. The computed pressures are compared to experiments for a swept wing and a nacelle. The full potential equation is used in Ref. 11. The configuration is a nacelle and a wing. Comparisons are made with measurements over the wing in Ref. 11. The slip-stream effects are modeled analytically using wind-tunnel data in Refs. 10 and 11. The Euler equations and a slip stream defined by experiments are solved over a wing in Ref. 12 and a nacelle-wing combination in Ref. 13. The calculated pressures are compared to experimental results on the wing.

In all the references above, the nacelle section is fairly small in comparison to the propeller disc, and there is no experimental validation of the computed nacelle pressures. Many of the methods are not satisfactory if the nacelle considerably modifies the slip-stream geometry behind the propeller. In most cases the calculations rely on experimental data or analytical approximations of the slip-stream properties. No velocities in the flowfield are compared to measurements. Only c_p values on the wing surfaces are compared to experimental data.

In the next section the physical and mathematical background for the slip-stream model is given. Then the computational method is described in Sec. III. The geometry of the slip stream is determined in the first step. In the second step, the singularity distribution in the slipstream is computed, the

Presented as Paper ICAS-90-5.4.4 at the 17th Congress of the International Council of the Aeronautical Sciences, Stockholm, Sweden, Sept. 9–14, 1990; received Jan. 27, 1991; revision received Sept. 21, 1991; accepted for publication Dec. 21, 1991.

*Research Scientist, Aerodynamics Department.

onset flow at the solid surfaces of the configuration is calculated, and then the panel method is invoked to obtain the complete flowfield. Comparisons with wind-tunnel experiments are made in Sec. IV. More comparisons are found in Ref. 14. The conclusions are drawn in the final section.

II. Background in Physics and Mathematics

This section is divided into two parts. We begin by deriving the basic relations for the representation of the vortical flow inside the slip stream. Then the blade element theory and the coupling to the slip-stream model are reviewed.

A. Slip-Stream Model

If we are interested in the time-average of the influence of the propeller on the downstream nacelle and wing surfaces, then the classical model replaces the discrete propeller blades by a continuum of propellers on a disk.[15] Therefore, the slip-stream consists of a continuum of propeller wakes and the velocity is a smooth time-independent variable.

Let $\mathbf{v}$ be the velocity of the flow

$$\mathbf{v} = (v_x, v_y, v_z)^T$$

Φ is a scalar potential and $\boldsymbol{A}$ is a vector potential. In incompressible flow it follows from the continuity equation that $\mathbf{v}$ is divergence-free

$$\nabla\cdot\mathbf{v} = 0 \tag{1}$$

By Helmholtz's decomposition theorem, $\mathbf{v}$ can be split into two parts $\mathbf{v}_1$ and $\mathbf{v}_2$ with the properties

$$\begin{aligned} \mathbf{v} &= \mathbf{v}_1 + \mathbf{v}_2 \\ \mathbf{v}_1 &= \nabla\times\boldsymbol{A}, \qquad \nabla\cdot\mathbf{v}_1 = 0 \\ \mathbf{v}_2 &= \nabla\Phi, \qquad \nabla\times\mathbf{v}_2 = 0 \end{aligned} \tag{2}$$

The rotational part of the flow in the slip stream is represented by $\mathbf{v}_1$ and $\boldsymbol{A}$ and the irrotational part, e.g., in the freestream, is represented by $\mathbf{v}_2$ and Φ. The potential Φ consists of two terms: 1) the freestream potential Φ_∞ and the potential due to the submerged body in the flow Φ_i:

$$\Phi = \Phi_\infty + \Phi_i \tag{3}$$

It follows from Eqs. (1) and (2) that

$$\nabla\cdot\mathbf{v} = \nabla\cdot\mathbf{v}_2 = \Delta\Phi = 0 \tag{4}$$

Equation (4) is solved for Φ by the panel method in Ref. 2. The method is of the same type as e.g., VSAERO[16] and PANAIR.[17] The boundary condition on Φ is a Dirichlet condition at the inner boundary of the configuration. This condition is usually chosen to be Φ_∞. Let (ξ, η, ζ) be a point on the configuration surface C and (x, y, z) an arbitrary point in space. Define

$$\mathbf{r} = (x-\xi, y-\eta, z-\zeta)^T$$

$$r = |\mathbf{r}| = \sqrt{(x-\xi)^2 + (y-\eta)^2 + (z-\zeta)^2}$$

and introduce the notation

$$\mathbf{b} = \nabla_\xi(1/r) = -\nabla_x(1/r) = \mathbf{r}/r^3$$

The differentiation in the operator ∇ is made with respect to the (x, y, z) or the (ξ, η, ζ) variables depending on the index. In the panel method[2] Φ_i in Eq. (3) is written as an integral over C of the surface singularity distributions $\mu_C(\xi, \eta, \zeta)$ (doublets) and $\sigma_C(\xi, \eta, \zeta)$ (sources and sinks)

$$\Phi_i(x, y, z) = \frac{1}{4\pi}\int_C (\mu_C\mathbf{n}\cdot\mathbf{b} - \sigma_C/r)\,dC \tag{5}$$

The boundary condition on the velocity $\mathbf{v}$ at the solid surfaces is

$$\mathbf{v}\cdot\mathbf{n} = \mathbf{v}_1\cdot\mathbf{n} + \mathbf{v}_2\cdot\mathbf{n} = 0 \tag{6}$$

where $\mathbf{n}$ is the normal of the surface. In Eq. (5) σ_C is equal to the jump in $\mathbf{v}\cdot\mathbf{n}$ at C. In the interior of C the velocity is

$$\mathbf{v}_1 + \nabla\Phi_\infty = \mathbf{v}_1 + \mathbf{v}_{2\infty}$$

Thus, by Eq. (6)

$$\sigma_C = -(\mathbf{v}_1 + \mathbf{v}_{2\infty})\cdot\mathbf{n} \tag{7}$$

The doublet distribution μ_C in Eq. (5) is determined so that Φ_i satisfies the Dirichlet condition

$$\Phi_i = 0 \tag{8}$$

in the interior of C.

The representation of the irrotational part of the flow is described above. We now turn to the vortical flow generated by the propeller. Let (ξ, η, ζ) be a point in the slip-stream Ω behind the propeller; introduce a volume doublet singularity distribution $\boldsymbol{\mu}(\xi, \eta, \zeta) \in \mathcal{R}^3$ in Ω and define $\boldsymbol{A}$ to be

$$\boldsymbol{A} = \frac{1}{4\pi}\int_\Omega \boldsymbol{\mu}\times\mathbf{b}\,d\Omega \tag{9}$$

Insert the identity

$$\nabla_\xi\times(\boldsymbol{\mu}/r) = \nabla_\xi\times\boldsymbol{\mu}/r + \mathbf{b}\times\boldsymbol{\mu}$$

into Eq. (9) and integrate by parts applying the following generalization of Gauss' theorem for an arbitrary vector $\boldsymbol{a}$

$$\int_\Omega \nabla_\xi\times\boldsymbol{a}\,d\Omega = \int_S \mathbf{n}\times\boldsymbol{a}\,dS$$

to obtain

$$\begin{aligned} \boldsymbol{A} &= \frac{1}{4\pi}\int_\Omega [\nabla_\xi\times\boldsymbol{\mu}/r - \nabla_\xi\times(\boldsymbol{\mu}/r)]\,d\Omega \\ &= \frac{1}{4\pi}\int_\Omega \nabla_\xi\times\boldsymbol{\mu}/r\,d\Omega - \frac{1}{4\pi}\int_S \mathbf{n}\times\boldsymbol{\mu}/r\,dS \end{aligned} \tag{10}$$

where S is the surface of Ω and $\mathbf{n}$ is its normal. With the volume and surface vorticity, Γ and Γ_S

$$\Gamma = \nabla_\xi\times\boldsymbol{\mu}, \qquad \Gamma_S = \mathbf{n}\times\boldsymbol{\mu} \tag{11}$$

the vector potential $\boldsymbol{A}$ in Eq. (10) can be written

$$\boldsymbol{A} = \frac{1}{4\pi}\int_\Omega \Gamma/r\,d\Omega - \frac{1}{4\pi}\int_S \Gamma_S/r\,dS \tag{12}$$

By Eq. (12) the rotational part of $\mathbf{v}$ is

$$\mathbf{v}_1 = \nabla_x\times\boldsymbol{A} = \frac{1}{4\pi}\int_\Omega \nabla_x\times(\Gamma/r)\,d\Omega - \frac{1}{4\pi}\int_S \nabla_x \times (\Gamma_S/r)\,dS \tag{13}$$

Introduce the relations

$$\nabla_x \times (\Gamma/r) = \nabla_x \times \Gamma/r + \nabla_x(1/r) \times \Gamma = -\mathbf{b} \times \Gamma$$

$$\nabla_x \times (\Gamma_S/r) = \Gamma_S \times \mathbf{b}$$

into Eq. (13) and we have derived the Biot-Savart law

$$\mathbf{v}_1 = \frac{1}{4\pi}\int_\Omega \Gamma \times \mathbf{b}\, d\Omega - \frac{1}{4\pi}\int_S \Gamma_S \times \mathbf{b}\, dS \qquad (14)$$

The vector potential $\boldsymbol{A}$ is solenoidal since

$$\nabla_x \cdot \boldsymbol{A} = \frac{1}{4\pi}\int_\Omega (\mathbf{b}\cdot\nabla_x \times \boldsymbol{\mu} - \boldsymbol{\mu}\cdot\nabla_x \times \mathbf{b})\, d\Omega = 0$$

One can show that

$$\nabla_x \times \mathbf{v} = \nabla_x \times \mathbf{v}_1 = \nabla_x \times \boldsymbol{\mu}(x, y, z) = \Gamma \qquad (15)$$

thus confirming the interpretation of Γ in Eq. (11) as a vorticity distribution.

We have found that the rotational flow with velocity $\mathbf{v}_1$ can be written as the curl of a vector potential $\boldsymbol{A}$. This potential $\boldsymbol{A}$ can be represented by a doublet density $\boldsymbol{\mu}$ in the volume Ω occupied by the slip stream where $\boldsymbol{\mu} \neq 0$ and $\nabla \times \mathbf{v}_1 \neq 0$, cf. Eqs. (9), (10), and (15). An alternative is to introduce a vorticity distribution Γ in Ω and Γ_S on S as in Eq. (14). The relation between Γ, Γ_S and $\boldsymbol{\mu}$ is given by Eq. (11).

The influence of $\boldsymbol{A}$ outside Ω is small so that $\mathbf{v}_1$ vanishes rapidly in $\mathcal{R}^3\backslash\Omega$. Moreover, we know from the theory of panel methods that

$$\lim_{r\to\infty} \nabla\Phi_i = 0$$

Thus, the correct boundary condition at ∞

$$\mathbf{v} = \nabla\Phi_\infty = \mathbf{v}_{2\infty}$$

outside Ω is satisfied. The boundary condition at the solid surfaces [Eq. (6)] is also fulfilled. The total velocity $\mathbf{v}$ is divergence-free [Eq. (1)]. We have a solution $\mathbf{v}$ that solves our problem.

The outline of the computational method is as follows:

1) Determine $\boldsymbol{\mu}$ in the slip-stream Ω or Γ in Ω and Γ_S on S by the combined momentum-blade element theory described in the next subsection.

2) Compute the rotational part $\mathbf{v}_1$ of the flow by Eqs. (14) and (11).

3) Insert $\mathbf{v}_1$ and the freestream speed $\mathbf{v}_{2\infty}$ into Eq. (7). Then solve the integral equation defined by Eqs. (8) and (5) for the doublet surface distribution μ_C.

4) Compute Φ in Eq. (3) and its gradient and use in Eq. (2) to obtain the total velocity $\mathbf{v}$. With Bernoulli's equation and the jump in the total pressure at the propeller disk, c_p can be calculated inside and outside the slip-stream Ω.

B. Momentum-Blade Element Theory and the Pressure Jump

The combined momentum- and simple-blade element theory employed to determine the vortex strength Γ generated at the propeller disk is described briefly in Ref. 14. For a detailed account see Refs. 3, 15, and 18. The angle ψ between the disk and the vortex filament leaving the trailing edge of the propeller blades is also given by the blade element theory.

According to incompressible propeller theory, the axial speed is continuous but the static pressure is discontinuous when the flow passes the propeller disk, (Ref. 3). Two different ways of obtaining the size of the pressure jump will be presented in the case when the freestream is parallel to the propeller axis.

Let the x axis in a cylindrical coordinate system coincide with the propeller axis and let the θ coordinate define the azimuthal position. The distance from the propeller axis is r. The components of $\mathbf{v}$ are

$$\mathbf{v} = (v_x, v_\theta, v_r)^T$$

In the first alternative, the thrust dT of an annulus at r is derived from the blade element theory. The corresponding pressure discontinuity Δp is

$$\Delta p = dT/(2\pi r\, dr) \qquad (16)$$

Using Eq. (16) the c_p coefficient is modified by a constant value Δc_p in each streamtube starting at the propeller disk. This value is determined at the disk to be

$$\Delta c_p = \Delta p/(\tfrac{1}{2}\rho v_{2\infty}^2) \qquad (17)$$

Far downstream in the fully contracted slip stream, the static pressure is equal to the freestream static pressure p_∞ (see Ref. 3). The second alternative is derived from this fact. The velocity in the slip stream far downstream is denoted by $\mathbf{v}_*$ and the constant density by ρ. Neglecting v_r it follows from Bernoulli's equation that

$$p_\infty + \tfrac{1}{2}\rho(v_{*x}^2 + v_{*\theta}^2) = p + \tfrac{1}{2}\rho(v_x^2 + v_\theta^2) \qquad (18)$$

in the slipstream. The pressure coefficient is by Eq. (18)

$$c_p = (p - p_\infty)/(\tfrac{1}{2}\rho v_{2\infty}^2) = [v_{*x}^2 + v_{*\theta}^2 - (v_x^2 + v_\theta^2)]/v_{2\infty}^2 \qquad (19)$$

Let w be the increase in speed at the disk in the x direction due to the propeller.

Introduce

$$v_{*x} = v_{2\infty} + 2w$$

into Eq. (19) to obtain

$$c_p = [v_{2\infty}^2 - (v_x^2 + v_\theta^2)]/v_{2\infty}^2 + [(2w)^2 + 4v_{2\infty}w + v_{*\theta}^2]/v_{2\infty}^2$$

$$= c_{p0} + [2 + (2w/v_{2\infty})](2w/v_{2\infty}) + (v_{*\theta}/v_{2\infty})^2 \qquad (20)$$

The usual pressure coefficient is c_{p0} in Eq. (20) and the last two terms correspond to Δc_p in Eq. (17).

III. Computational Model

The solution process is split into two separate steps which are independent of each other. First, the outer boundary and the inner structure of the slipstream is generated by following streamlines starting at the propeller disk. These streamlines are computed by the panel method.[2] In the second step the flowfield about the configuration is determined following the outline at the end of Sec. II.A.

The coordinate system in this section is the same cylindrical system as in Sec. II.B. The propeller axis is a part of the x axis and freestream flow perpendicular to the propeller disk has $\alpha = 0$ deg.

A. Slip-Stream Discretization

The slip-stream Ω is divided into a number of nonoverlapping cells ("field panels") ω_{ijk}, $i = 1, \ldots, l$, $j = 1, \ldots, m$, $k = 1, \ldots, n$, (see Fig. 1). The index i runs in the x direction, j in the positive θ direction, and k in the r direction. The slipstream is unbounded in the positive x direction, but in the computations the slipstream is extended to $x = x_{end}$ only, so that l and the volume of each ω_{ijk} are finite. If x_{end} is chosen

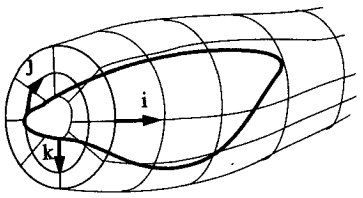

Fig. 1 Discretization of the slip stream around a nacelle.

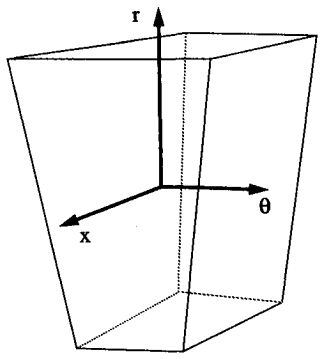

Fig. 2 Field panel ω_{ijk} and its local coordinate system.

sufficiently far downstream, then the influence of this limit is small on the flow in the neighborhood of the configuration. Then Ω can be written

$$\Omega = \bigcup_{\substack{i=1,l \\ j=1,m \\ k=1,n}} \omega_{ijk}$$

The cells ω_{ijk} are distorted cubes defined by their eight corners (see Fig. 2). There is a doublet density μ_{ijk} associated with each ω_{ijk}.

In order to compute μ_{ijk} a number of simplifications are introduced. A vortex tube is defined by a number of vortex filaments in the same way as streamlines define a stream tube. According to the first vortex theorem[19] the circulation around a vortex tube is constant along the tube. If B is an arbitrary cross section of the tube and ∂B is its boundary, then by Stokes' theorem and Eq. (15)

$$\int_{\partial B} \mathbf{v}\cdot d\mathbf{l} = \int_B (\nabla \times \mathbf{v})\cdot \mathbf{n}\, dB = \int_B \Gamma\cdot \mathbf{n}\, dB$$

$$= \int_B (\nabla \times \boldsymbol{\mu})\cdot \mathbf{n}\, dB = \int_{\partial B} \boldsymbol{\mu}\cdot d\mathbf{l} = \text{const} \qquad (21)$$

Consider the cylindrical surface generated by a set of streamlines leaving the propeller disk at distance r from the axis and the corresponding surface generated by the vortex filaments. At $\alpha = 0$ deg the assumption is that these two surfaces remain identical downstream of the disk. Furthermore, at $\alpha = 0$ deg the vorticity created by the propeller is independent of θ. Since B is arbitrary in Eq. (21) it follows that if $\alpha = 0$ deg and the angle between the streamlines and the vortex filaments is constant on each surface, then Eq. (21) is true also for the stream tubes from the propeller. The circumference of a stream tube is almost constant. Therefore, by Eq. (21) our first simplification is

$$\mu_{ijk} = \mu_{jk}, \quad i = 1, \ldots, l \qquad (22)$$

i.e., μ is constant in the stream tubes from the propeller. At $\alpha = 0$ deg we have in addition

$$\mu_{jk} = \mu_k, \quad j = 1, \ldots, m \qquad (23)$$

We now turn to the components of μ_{jk} defined in the local cartesian coordinate system in Fig. 2.

$$\boldsymbol{\mu}_{jk} = (\mu_{jkx}, \mu_{jk\theta}, \mu_{jkr})^T$$

The axes of the local system in each cell are not always completely aligned with the axes of the global cylindrical system. It follows from analogy with wing-wakes that μ_{jkr} is small. The first component μ_{jkx} is taken to be constant in ω_{ijk}. For reasons to be explained later, we choose a linear variation of $\mu_{jk\theta}$ in the radial direction in ω_{ijk}. Let r_0 and r_1 be the local r coordinate of the bottom and top surface of ω_{ijk} in Fig. 2. The widths of these surfaces in the local θ direction are t_0 and t_1, respectively. Then

$$\mu_{jk\theta}(r) = \hat{\mu}_{jk\theta} f(r)$$

$$f(r) = 1 + \frac{r - r_0}{r_1 - r_0}\left(\frac{t_0}{t_1} - 1\right) \qquad (24)$$

The velocity $\mathbf{v}_{ijk}$ at a point (x, y, z) induced by μ_{jk} in cell ω_{ijk} with surface s_{ijk} is by Eq. (14)

$$\mathbf{v}_{ijk} = \frac{1}{4\pi}\int_{\omega_{ijk}} \Gamma_{jk} \times \mathbf{b}\, d\omega - \frac{1}{4\pi}\int_{s_{ijk}} \Gamma_{sjk} \times \mathbf{b}\, ds \qquad (25)$$

With definitions analogous to Eq. (11) $\mathbf{v}_{ijk}$ can also be written

$$\mathbf{v}_{ijk} = \frac{1}{4\pi}\int_{\omega_{ijk}} (\nabla \times \boldsymbol{\mu}_{jk}) \times \mathbf{b}\, d\omega$$

$$- \frac{1}{4\pi}\int_{s_{ijk}} (\mathbf{n} \times \boldsymbol{\mu}_{jk}) \times \mathbf{b}\, ds \qquad (26)$$

Rewrite the first integral in Eq. (25) in the same way as Eq. (9) is rewritten to Eq. (10). It follows from Eq. (24) that Γ_{jk} is constant in ω_{ijk}. Thus

$$\nabla \times \Gamma_{jk} = 0$$

We have arrived at a new expression for $\mathbf{v}_{ijk}$ without volume integrals

$$\mathbf{v}_{ijk} = -\frac{1}{4\pi}\int_{s_{ijk}} (\mathbf{n} \times \Gamma_{jk}/r + \Gamma_{sjk} \times \mathbf{b})\, ds \qquad (27)$$

The volume integral in Eq. (26) has been transformed to a surface integral [Eq. (27)].

We simplify the representation of the slip-stream vorticity further by only taking the contribution from Γ_{sjk} in Eq. (27) into consideration. The interpretation of this is that there is a surface distribution of vorticity

$$\Gamma_{sjk} = \mathbf{n} \times \boldsymbol{\mu}_{jk}$$

on each cell face. There is an important computational advantage in using surface vorticity instead of discrete vortex filaments. The velocity is singular at the center of a filament but only the derivative of the velocity is singular when a vortex surface is crossed.

Since we let $\mu_{jkr} = 0$ and $\mu_{jk\theta}$ is constant in the x direction in a stream tube, the singularities on the cell faces $x \approx$ const will cancel except for the face on the propeller disk. The contribution from the faces with $\theta \approx$ const will also cancel if the μ_{jk} density is constant in the azimuthal direction and is small if $\alpha \neq 0$ deg. The vorticity density Γ_{sjk} is approximately constant on the surfaces t_{ijk} where $r \approx$ const. Therefore, by Eq. (27)

$$\mathbf{v}_{ijk} \approx -\frac{1}{4\pi}\Gamma_{sjk} \times \int_{t_{ijk}} \mathbf{b}\, ds \qquad (28)$$

The advantage with the surface integral in Eq. (28) is that the same subroutines that were developed for the evaluation of the integrals in the panel program[2] can be reused.

The induced velocities caused by the vorticity on the faces with $r \approx$ const

$$\Gamma_{sjk} = \begin{bmatrix} \Gamma_{sjkx} \\ \Gamma_{sjk\theta} \\ \Gamma_{sjkr} \end{bmatrix} \approx \delta \begin{bmatrix} -\mu_{jk\theta} \\ \mu_{jkx} \\ 0 \end{bmatrix}, \quad \delta = \begin{cases} 1, & r = r_1 \\ -1, & r = r_0 \end{cases}$$

cannot be neglected. At the bottom of the cell in Fig. 2 we have

$$\Gamma_{sjkx} = \hat{\mu}_{jk\theta}$$

and at the top

$$\Gamma_{sjkx} = -\hat{\mu}_{jk\theta} t_0/t_1$$

The choice of $\boldsymbol{\mu}_{jk}$ in Eq. (24) is motivated by the second vortex theorem in Ref. 19 applied to each cell. The amount of vorticity on the bottom face $\Gamma_{sjkx}t_0$ in the x direction appears on the top face in the opposite direction. Suppose that for each column of cells in a stream tube t_0 and t_1 are constant. Since the vorticity of every cell ω_{ijk} has the above property, then the whole slip-stream Ω satisfies the second vortex theorem,[19] i.e., a vortex filament never ends in the fluid but closes onto itself, and ends at a boundary or goes to infinity.

The system of helical vortices in the slip stream is modeled by a vorticity Γ_s on cylindrical surfaces starting at the propeller disk. The vorticity is composed of ring vortices $\Gamma_{s\theta}$ and axial vorticity Γ_{sx}. It follows from Eq. (28) that $\Gamma_{s\theta}$ is responsible for most of the acceleration of $\mathbf{v}$ in the x direction and Γ_{sx} for the swirl in the θ direction.

The vorticity Γ from the combined momentum-blade element theory in Sec. II.B. is transferred to the surface vorticity Γ_s in Eq. (28) in the following way. After the simplifications above we are interested in Γ_{sjk} on cylinders starting with a circular section at the propeller and following the streamlines from the disk. Let the direction of the discrete vortex filament be $\mathbf{l}$ from the trailing edge of the propeller blade. The vorticity shed over the distance $r\,\mathrm{d}\theta$ is $\Gamma\, r\,\mathrm{d}\theta$. The surface corresponding to a vortex of length $\mathrm{d}\mathbf{l}$ is $\mathrm{d}x\, r\,\mathrm{d}\theta$. The angle is ψ between the filament and the disk (cf. Sec. II.B.). Then the surface density $(\Gamma_x, \Gamma_\theta)$ is

$$\Gamma r\,\mathrm{d}\theta\,\mathrm{d}\mathbf{l} = \begin{bmatrix} \Gamma \sin\psi \\ \Gamma\cos\psi \end{bmatrix} r\,\mathrm{d}\theta(r\,\mathrm{d}\theta/\cos\psi)$$

$$= \begin{bmatrix} \Gamma\tan\psi \\ \Gamma \end{bmatrix} (r\,\mathrm{d}\theta)^2 = \begin{bmatrix} \Gamma \\ \Gamma/\tan\psi \end{bmatrix} \mathrm{d}x\, r\,\mathrm{d}\theta$$

$$= \begin{bmatrix} \Gamma_x \\ \Gamma_\theta \end{bmatrix} \mathrm{d}x\, r\,\mathrm{d}\theta$$

The level of approximation in the panel method is low with flat panels and constant σ_C and μ_C on each panel. Compressibility effects are approximated by the Göthert rule.

B. Slip-Stream Geometry

In the previous subsection the representation of the rotational flow in the discretized slip stream by means of singularity distributions was described. We continue with the generation of the cylinders defining the geometry of the slip-stream Ω. Different choices of Ω are possible and this choice is independent of the representation in Sec. III.A.

The simplest slip-stream geometry consists of a number of concentric cylinders with their center on the propeller axis and radius r_k, $k = 0, \ldots, n$. This is the strategy adopted in many of the papers referred to in Sec. I. The influence of the slipstream on the nacelle is not very accurate in this approach. A more ambitious model is to let both the nacelle and the wing participate in the shaping of the cylinders. This will probably be a rather complicated process (see Ref. 20). We have chosen a middle way between these two extremes by letting the propeller disk, the nacelle surface, and a trailing sting determine the geometry of the slip stream. The sting is added to the base of the nacelle to model the flow better in that region and to simulate wind-tunnel conditions.

The cylinder surfaces in the slip-stream geometry are the stream surfaces emanating from circles on the propeller disk. The streamlines defining the stream surfaces are calculated by the panel method.[2] If the velocity component $\mathbf{v}_1$ from the slipstream is small in comparison to $\mathbf{v}_2$ then the generated stream surfaces are fairly representative of the true stream surfaces in Ω. Note that if $\alpha = 0$ deg then there is no need to follow the θ or swirl component of the streamlines, since $\boldsymbol{\mu}_{jk}$ and Γ_{jk} are constant for $j = 1, \ldots, m$.

The slip-stream cylinders are partitioned into panels. The velocity $\mathbf{v}_1$ due to the slip stream is computed at the midpoint of every cell ω_{ijk}. This velocity is the sum of the contributions from the singularity densities in all the cells in Ω. By linear interpolation between the velocities $\mathbf{v}_{1ijk}$ at the midpoints, $\mathbf{v}_1$ at an arbitrary point (e.g., the panel midpoints of the configuration surface) can be computed.

The extra work required by a user to simulate the influence of propeller slip stream around an existing paneled configuration is negligible with our present implementation of the method. In a recent application with a wing-body geometry the CPU time on a CRAY X-MP increased by about 20% when including the slip-stream effects.

IV. Computational Results and Comparisons

In the low-speed wind-tunnel experiments in Refs. 4 and 5 two configurations with a wing are tested. One model has an axisymmetric nacelle and a straight wing with symmetric profile mounted symmetrically on the nacelle. The other model has the same wing but the nacelle is nonaxisymmetric with the propeller axis located over the wing. A description of the geometry of the models is found in Ref. 4. The pressures and velocities around these configurations computed by CRAY X-MP are compared to the measured values in this section.

The axisymmetric nacelle and its wing are paneled in Fig. 3. The propeller has four blades and its position and size are depicted in the top of Fig. 5. The wing profile is *NACA* $63_{(10)}A$—012. The discontinuity in the static pressure at the propeller disk is determined by the condition on the presssure in the fully contracted slipstream (see Sec. II.B.).

The geometry of the wind-tunnel model of the nonaxisymmetric nacelle and its wing is modified in the computations for the following reason. The slip-stream model in Sec. III.B. assumes that no streamlines from the propeller disk hit the nacelle surface. This does not seem to be the case with the original geometry. The frontal part of the nacelle is therefore

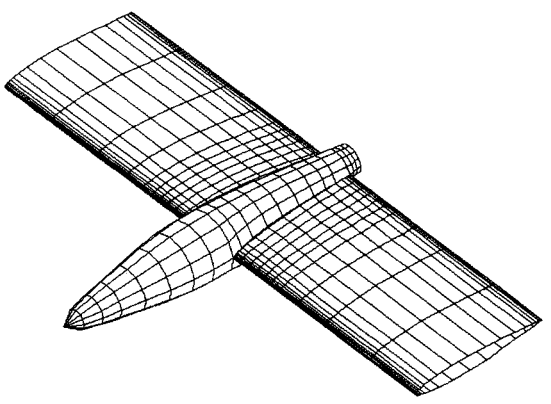

Fig. 3 Discretization of the axisymmetric nacelle with wing.

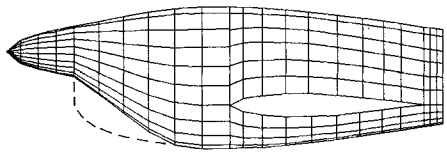

Fig. 4 Side view of the modified geometry of the nonaxisymmetric nacelle with wing.

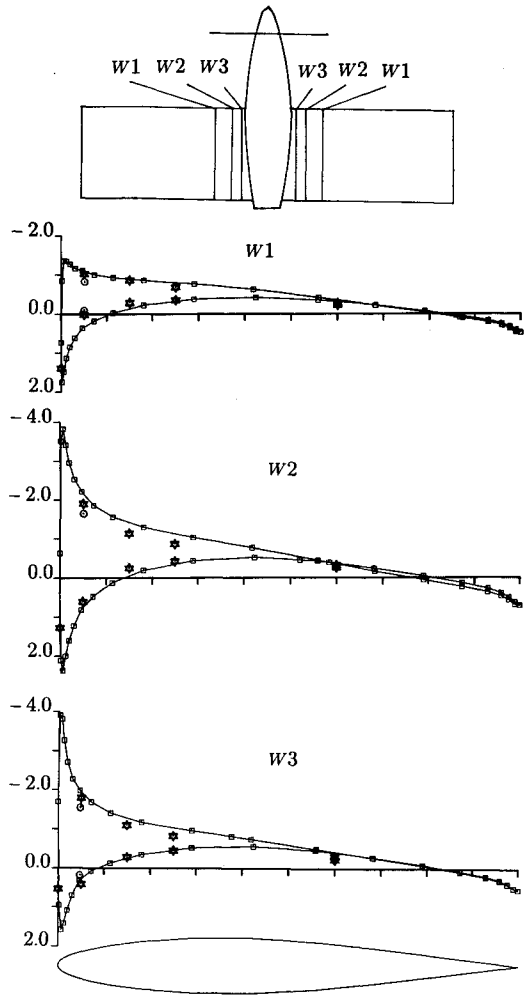

Fig. 5 Comparison of c_p values at $\alpha = 0$ deg on the wing with the axisymmetric nacelle.

changed to suit the computations better, (see Fig. 4). The dashed line in Fig. 4 represents the wind-tunnel geometry. The assumption is that the flow over the wing is not altered very much by this change of geometry. The propeller and wing profile are the same as above. The paneling of the wing is the same as in Fig. 3.

The cylindrical surfaces representing the slip-stream geometry are generated around the nacelles without wings (cf. Sec. III.B.). The Mach number in the experiments and the computations is 0.15. The propeller thrust coefficient C_T and the advance ratio J are defined by

$$C_T = T/(\rho_\infty N^2 D^4), \quad J = v_\infty/(ND)$$

where T is the thrust, N is the rotational speed of the propeller, and D is the diameter. The value of C_T is about 0.22 and J is 0.70.

In the first example, the pressures on the axisymmetric nacelle and its wing are computed and compared to the experimental values. The propeller rotates in the negative θ direction. At $\alpha = 0$ deg the flowfield is antisymmetric around

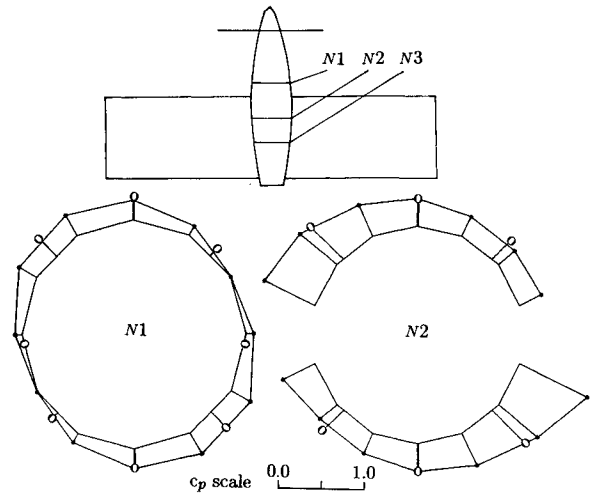

Fig. 6 Comparison of c_p values at $\alpha = 0$ deg on the axisymmetric nacelle.

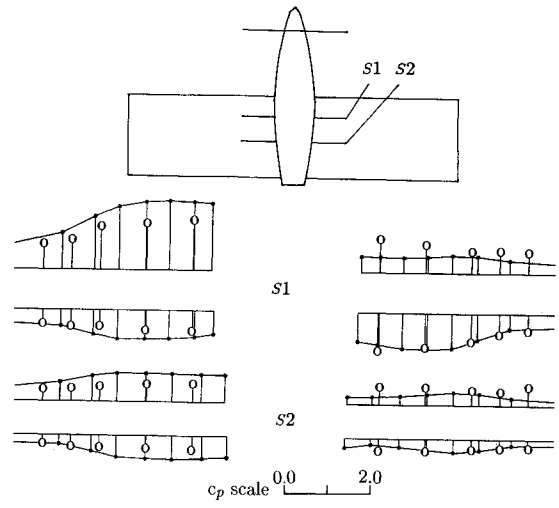

Fig. 7 Comparison of c_p values at $\alpha = 0$ deg on the wing with the nonaxisymmetric nacelle.

the propeller axis. The flow above the starboard wing is identical to the flow below the port wing and vice versa. This antisymmetry is reproduced very well in the computations. The antisymmetry is not perfect in the wind-tunnel data. In Fig. 5 the c_p values at three sections of the port wing are compared. If the two measured values from the starboard (⊙) and port (★) wing that should be equal are a little apart, then both values are plotted and combined by a line. The symbol for the computed data is □. The computed sectional lift coefficients of the wing inside the slip stream will be greater than the corresponding measured coefficients.

The nacelle pressures are displayed at two nacelle sections in Fig. 6 looking upstream. The length of an arrow is proportional to the c_p value at its foot. The symbol * denotes a computed and ○ a measured value. The symbols on the arrows are placed at the nacelle surface if c_p is positive, and away from the surface if c_p is negative. The agreement between calculated and experimental data is good in this case.

The c_p values for the nonaxisymmetric nacelle and the wing at $\alpha = 0$ deg are plotted and compared in Figs. 7 and 8. The arrows and symbols have the same interpretation as in Fig. 6. The port side is to the left and the starboard side is to the right in the c_p plots in Fig. 7. The extension of these plots in the r direction is indicated in the configuration overview at the top. The nacelle sections in Fig. 8 are defined in Fig. 6. The effect of the slip stream is overestimated in the computations in comparison to the experiments.

The results at $\alpha = 5$ deg for the axisymmetric configuration are shown in Figs. 9 and 10. The c_p values on the wing and the nacelle are plotted as in Figs. 7 and 8 with the same definitions of the configuration sections. We have chosen the same slip-stream geometry as in the case $\alpha = 0$ deg, but the momentum-blade element theory is modified to handle an α different from 0. Also here the effect of the slipstream on the wing is greater in the calculated values than in the measured values.

The velocities in the flowfield outside the axisymmetric nacelle are compared in Fig. 11 at $\alpha = 0$ deg. The computed velocities (○) are compared with the experimental velocities (·) along a ray in the vertical direction starting at the nacelle surface at section $N2$ in Fig. 6. The velocities are proportional to the abscissa in Fig. 11. Note that the abscissa scales are different in the v_x and the v_θ plots. The ordinate is the distance r from the propeller axis scaled by the propeller radius r_p. The difference between the calculated and measured velocities are of the same order in the x and θ directions.

There are several possible explanations to the discrepancies between the computed and the experimental data. This matter is discussed in Ref. 14. Finally, we remark that there are errors also in the wind-tunnel experiments. The deviation from antisymmetry for the axisymmetric nacelle $\alpha = 0$ deg provides a measure of that uncertainty.

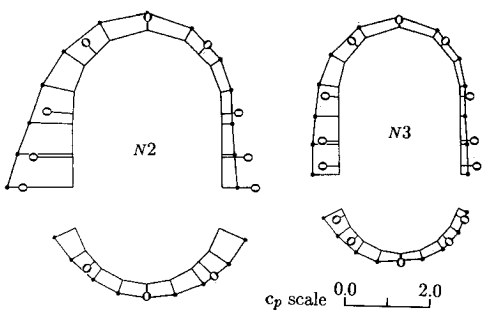

Fig. 8 Comparison of c_p values at $\alpha = 0$ deg on the nonaxisymmetric nacelle.

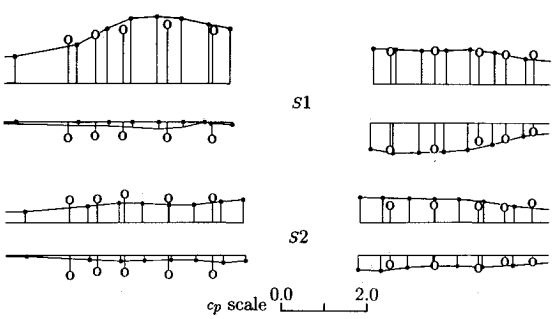

Fig. 9 Comparison of c_p values at $\alpha = 5$ deg on the wing with the axisymmetric nacelle.

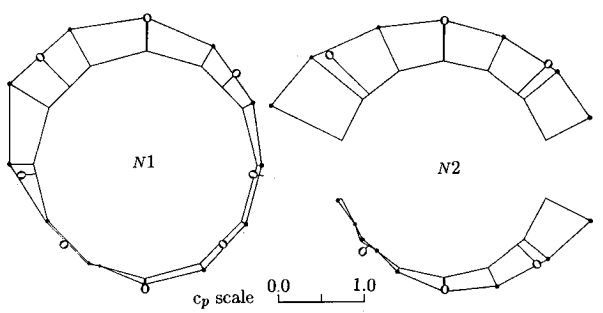

Fig. 10 Comparison of c_p values at $\alpha = 5$ deg on the axisymmetric nacelle.

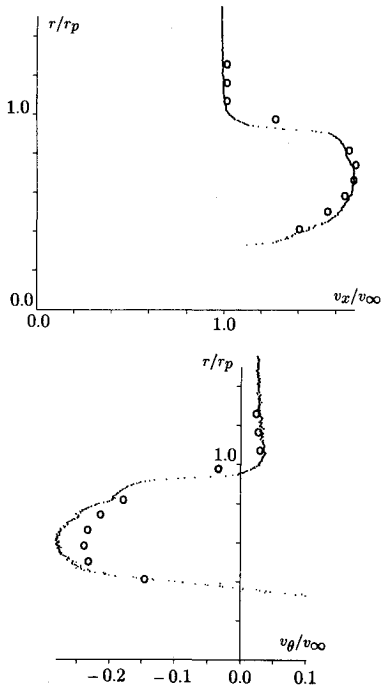

Fig. 11 Velocities at $\alpha = 0$ deg in the flowfield around the axisymmetric nacelle with wing.

V. Conclusions

A computational model of the slip stream behind a propeller has been developed and implemented in an existing panel program environment. The vortical flow in the slip stream is represented by a surface vorticity distribution Γ_S on cylindrical surfaces approximating the internal structure of the slip stream. The vorticity Γ_S is computed by a combined momentum-blade element theory. The calculations are compared to wind-tunnel results for two configurations: 1) an axisymmetric nacelle with a wing; and 2) a nonaxisymmetric nacelle with a wing. In the first case at $\alpha = 0$ deg the computed pressures and velocities agree well with the experiments. The influence of the slip stream on the c_p values on the surfaces of the nonaxisymmetric configuration is greater in the computations in comparison with the measurements. The results for the axisymmetric nacelle at $\alpha = 5$ deg are good on the nacelle and of the same quality on the wing as in the nonaxisymmetric case.

Acknowledgment

The author has had many fruitful discussions with Bert Arlinger on the subject of this paper.

References

[1]Hoeijmakers, H. W. M., "Panel Methods in Aerodynamics; Some Highlights," *Panel Methods in Fluid Mechanics with Emphasis on Aerodynamics*, edited by J. Ballmann, R. Eppler, and W. Hackbusch, Vol. 21, *Notes on Numerical Fluid Mechanics*, Vieweg, Braunschweig, Germany, 1988, pp. 1–34.

[2]Lötstedt, P., "Evaluation of a Higher Order Panel Program for Subsonic Flow, *Panel Methods in Fluid Mechanics with Emphasis on Aerodynamics*, edited by J. Ballmann, R. Eppler, and W. Hackbusch, Vol. 21, *Notes on Numerical Fluid Mechanics*, Vieweg, Braunschweig, Germany, 1988, pp. 147–155.

[3]McCormick, B. W., Jr., *Aerodynamics of V/STOL Flight*, Academic Press, New York, 1967, pp. 73–82.

[4]Samuelsson, I., "Low Speed Wind Tunnel Investigation of Propeller Slipstream Aerodynamic Effects on Different Nacelle/Wing Combinations," ICAS Paper 88-4.11.1, Jerusalem, Israel, Aug. 1988.

[5]Samuelsson, I., "Experimental Investigation of Low Speed Model Propeller Slipstream Aerodynamic Characteristics Including Flow Field Surveys and Nacelle/Wing Static Pressure Measurements," ICAS Paper 90-3.1.3, Stockholm, Sweden, Sept. 1990.

[6]Aljabri, A. S., "Aerodynamic Design of Propfan Powered Transports," AIAA Paper 83-1213, Seattle, WA, June 1983.

[7]Clark, R. W., and Valarezo, W. O., "Subsonic Calculation of Propeller/Wing Interference," AIAA Paper 90-0031, Reno, NV, Jan. 1990.

[8]Hess, J. L., and Valarezo, W. O., "Calculation of Steady Flow About Propellers Using a Surface Panel Method," *Journal of Propulsion and Power*, Vol. 1, No. 6, 1985, pp. 470–476.

[9]Valarezo, W. O., "Calculation of Isolated and Installed Multiple Rotor Flows Using a Surface Panel Method," AIAA Paper 89-2214, Seattle, WA, July 1989.

[10]Boppe, C. W., and Rosen, B. S., "Computation of Prop-Fan Engine Installation Aerodynamics," *Journal of Aircraft*, Vol. 23, No. 4, 1986, pp. 299–305.

[11]Samant, S. S., Yu, N. J., and Rubbert, P. E., "Transonic Flow Simulation of Prop-Fan Configurations," AIAA Paper 83-0187, Reno, NV, Jan. 1983.

[12]Whitfield, D. L., and Jameson, A., "Three-Dimensional Euler Equation Simulation of Propeller-Wing Interaction in Transonic Flow," AIAA Paper 83-0236, Reno, NV, Jan. 1983.

[13]Samant, S. S., and Yu, N. J. "Flow Prediction for Propfan Engine Installation Effects on Transport Aircraft at Transonic Speeds," NASA CR 3954, 1986.

[14]Lötstedt, P., "A Propeller Slipstream Model in Subsonic Linearized Potential Flow," ICAS Paper 90-5.4.4, Stockholm, Sweden, Sept. 1990.

[15]Glauert, H., "Airplane Propellers," *Aerodynamic Theory*, edited by W. F. Durand, Vol. IV, Springer-Verlag, Berlin, 1935.

[16]Maskew, B., "Prediction of Subsonic Aerodynamic Characteristics: A Case for Low-Order Panel Methods," *Journal of Aircraft*, Vol. 19, No. 2, 1982, pp. 157–163.

[17]Carmichael, R. L., and Erickson, L. L., "PANAIR—A Higher Order Panel Method for Predicting Subsonic or Supersonic Linear Potential Flows About Arbitrary Configurations," AIAA Paper 81-1255, Palo Alto, CA, June 1981.

[18]Lock, C. N. H., Pankhurst, R. C., and Conn, J. F. C., "Strip Theory Method of Calculation for Airscrews on High-Speed Aeroplanes," Aeronautical Research Council Technical Rept., His Majesty's Stationery Office, R. & M. 2035, London, 1945.

[19]Ashley, H., and Landahl, M., *Aerodynamics of Wings and Bodies*, Addison-Wesley, Reading, MA, 1965, pp. 7–9.

[20]Clark, D. R., "The Use of Panel Methods in the Calculation of the Flows Around General Configurations Including the Coupled Effects of Rotors and Propellers," *Proceedings of Computational Fluid Dynamics in Aerospace Design Workshop*, Univ. of Tennessee Space Inst., Tullahoma, TN, 1985, pp. 11.0–11.34.